Nanoscale

PAPER

View Article Online
View Journal | View Issue

Cite this: *Nanoscale*, 2016, **8**, 12294

Highly transparent, low-haze, hybrid cellulose nanopaper as electrodes for flexible electronics†

Xuezhu Xu,[a,b,c] Jian Zhou,[c] Long Jiang,*[a,b] Gilles Lubineau,*[c] Tienkhee Ng,[d] Boon S. Ooi,[d] Hsien-Yu Liao,[d] Chao Shen,[d] Long Chen[e] and J. Y. Zhu[f]

Received 17th March 2016,
Accepted 31st May 2016

DOI: 10.1039/c6nr02245f

www.rsc.org/nanoscale

Paper is an excellent candidate to replace plastics as a substrate for flexible electronics due to its low cost, renewability and flexibility. Cellulose nanopaper (CNP), a new type of paper made of nanosized cellulose fibers, is a promising substrate material for transparent and flexible electrodes due to its potentially high transparency and high mechanical strength. Although CNP substrates can achieve high transparency, they are still characterized by high diffuse transmittance and small direct transmittance, resulting in high optical haze of the substrates. In this study, we proposed a simple methodology for large-scale production of high-transparency, low-haze CNP comprising both long cellulose nanofibrils (CNFs) and short cellulose nanocrystals (CNCs). By varying the CNC/CNF ratio in the hybrid CNP, we could tailor its total transmittance, direct transmittance and diffuse transmittance. By increasing the CNC content, the optical haze of the hybrid CNP could be decreased and its transparency could be increased. The direct transmittance and optical haze of the CNP were 75.1% and 10.0%, respectively, greatly improved from the values of previously reported CNP (31.1% and 62.0%, respectively). Transparent, flexible electrodes were fabricated by coating the hybrid CNP with silver nanowires (AgNWs). The electrodes showed a low sheet resistance (minimum 1.2 Ω sq^{-1}) and a high total transmittance (maximum of 82.5%). The electrodes were used to make a light emitting diode (LED) assembly to demonstrate their potential use in flexible displays.

1. Introduction

Flexible, highly transparent and conductive electrodes are required in next-generation flexible electronics in applications such as flexible large-area displays, touch screens,[1] LED light sources[2] and solar energy devices.[3] Indium tin oxide (ITO) has long been used to make glass-based transparent electrodes. The drawbacks of these traditional electrodes are numerous: they are brittle[4] and expensive; they are made from limited/non-renewable raw materials; their manufacturing processes are environmentally damaging. ITO-based electrodes are not well suited to flexible electronics because the channel cracking in the brittle ITO coating during fracture dramatically decreases the conductivity of the electrodes, rendering them non-operational. Poly(3,4-ethylenedioxythiophene)/polystyrene sulfonate (PEDOT/PSS),[5,6] carbon nanotubes (CNTs), graphene and silver nanowires (AgNWs)[7–10] have been coated on flexible polymer substrates with the aim of replacing ITO/glass electrodes. These new flexible electrodes not only exhibit comparable optical properties but also offer additional advantages including light weight, stretchability, high electrical conductivity,[11] and good processibility (*e.g.*, they are rollable, heatable and printable). However, the commonly used polymer substrate materials, *e.g.*, polyethylene terephthalate (PET), polyimide (PI), and various fluoropolymers, are all made from petroleum-based chemicals. Environmental concerns and uncertainties about oil price and availability have made it an increasingly attractive option to produce the materials from bioresources.[12] Very recently, flexible electronics on cellulose nanopaper substrate have been developed.[13] The nanopaper substrate is made using a method similar to the traditional paper making process. However, rather than using microsized cellulose fibers in traditional paper, cellulose nanofibers isolated from lignocellulosic biomass are used to produce the nanopaper.

Two types of cellulose nanofibers have been produced from various bio-resources. One is cellulose nanofibrils (CNFs),

[a]*North Dakota State University, Department of Mechanical Engineering, USA*
[b]*Program of Materials and Nanotechnology, Fargo, ND 58102, USA. E-mail: long.jiang@ndsu.edu*
[c]*King Abdullah University of Science and Technology (KAUST), Physical Science and Engineering Division, Mechanical Engineering, COHMAS Laboratory, Thuwal 23955-6900, Saudi Arabia. E-mail: gilles.lubineau@kaust.edu.sa*
[d]*King Abdullah University of Science and Technology (KAUST), Physical Science and Engineering Division, Electrical Engineering, Photonics Laboratory, Thuwal 23955-6900, Saudi Arabia*
[e]*King Abdullah University of Science and Technology (KAUST), Advanced Nanofabrication, Imaging and Characterization Core Laboratory, Thuwal 23955-6900, Saudi Arabia*
[f]*Forest Products Laboratory, USDA Forest Service, Madison, Wisconsin 53726, USA*
†Electronic supplementary information (ESI) available. See DOI: 10.1039/C6NR02245F

which are long, flexible, often-entangled fibrils containing both crystalline and amorphous cellulose. The other is needle-shaped cellulose nanocrystals (CNCs), a product from acid hydrolysis of cellulosic fibers to remove amorphous cellulose. CNFs can be isolated from different types of lignocellulosic biomass through direct mechanical fibrillation,[14,15] mechanical fibrillation after enzymatic hydrolysis,[16,17] mechanical fibrillation after 2,2,6,6-tetramethylpiperidine-1-oxyl radical (TEMPO)-mediated oxidation,[18] carboxymethylation[19] or acid treatment.[20] Production of CNCs generally involves hydrolysis of cellulosic fibers by strong acids (*e.g.*, sulfuric and hydrochloride acids).[21] While wood pulp is the most widely used feedstock to produce cellulose nanofibers, many other natural fibers have also been used.[22] A recent review paper describes various production methods for CNFs and CNCs.[23,24] Research on cellulose nanofibers has grown in recent years due to their high strength, high modulus, large aspect ratio/surface area, low density, rich surface chemistry (*i.e.* various chemical surface modification methods), optical properties, and renewability.[13,25–28]

CNC- or CNF-reinforced polymer sheets and cellulose nanopaper (CNP) have been tested as substrates for transparent and flexible electrodes.[13,13,29–36] For the first type, the cellulose nanofibers are used as reinforcements in polymers to produce transparent composite substrates.[37–39] For the second type, all-CNF CNP (based on either unmodified or TEMPO modified CNFs) as a transparent substrate has been developed using a filtration and pressing process.[16,29,30,40] Compared to polymer based substrates, CNP shows the advantage of high thermal stability. For example, Hsieh *et al.* found that the thermal degradation temperature of CNP was 300 °C. No color change and dimensional changes (*e.g.* shrinking, warping, twisting, *etc.*) were observed after 30 min at 200 °C.[41] While the mechanical/thermal properties and transparency of the CNP are very competitive, many of the products also exhibit high optical haze, which results from strong diffuse transmittance caused by light scattering from large nanofiber bundles and/or pores within the nanopaper.[11,31,41,42]

The total transparency, T_{total}, of a medium is defined as the ratio of transmitted radiant power to incident radiant power. It is the sum of the direct transmittance, T_{direct}, and the diffuse transmittance, $T_{diffuse}$ such that $T_{total} = T_{direct} + T_{diffuse}$. The percentage, defined as $T_{diffuse}/T_{total} \times 100\%$, quantifies the ratio of light that is transmitted in a diffuse manner and is a measurement of optical haze. The CNP prepared by Hu's group has a T_{total} up to 90% (at 600 nm wavelength) and a T_{direct} as low as ~20%, resulting in a product with high transparency but also high haze.[11,37,43–46] Nogi *et al.* showed that the scattering (and consequently the haze) can be largely decreased by polishing or coating the surface of the nanopaper (T_{direct} increased to 71.6% after the treatments).[46] While high haze is a useful feature for applications such as skylights, indoor lighting and solar cells,[31] which often benefit from diffuse transmittance, CNP with high haze is not suitable for applications that require high transparency and clarity, *e.g.*, flexible displays and touch screens.

An extensive literature review reveals that current free-standing transparent nanopaper substrates are mostly based on wood-based CNFs or a mixture of CNFs and micro-sized cellulose fibers, and many of them exhibit high haze.[13,31,41,44,47,48] TEMPO-oxidation of CNFs has been shown to refine the nanofibers and therefore produce CNP with improved transparency and haze.[16,35,42,48–51] Yet, it is still difficult to tailor the optical properties of the obtained CNP for different applications. Our goal in this study is to develop a facile method to produce CNP with a wide range of optical properties using CNFs and CNCs simultaneously. By varying the CNC/CNF ratio, we can control the transparency and haze of the hybrid CNP. We demonstrate its application as a transparent electrode by coating it with a layer of silver nanowires (AgNWs). The electrode exhibits high electrical conductivity that is stable under large bending deformation, which satisfies the requirement for flexible/wearable electronics.

2. Materials and methods

2.1. Materials

The CNCs and CNFs were produced from a dry lap bleached kraft eucalyptus pulp at USDA Forest Service, Forest Products Laboratory, Madison, WI. The CNCs were produced by acid hydrolysis using sulfuric acid of 58 wt% at 56 °C for 100 min as described previously.[52] The acid form of the resultant CNCs was used for the present study with a sulfur content of 6.8 mg g^{-1} and a surface charge (zeta potential) of −45 mV measured by a zeta potential analyzer (Nanobrook Omni, Brookhaven Instruments, Holtsville, NY) based on monitoring electrophoretic mobility using Phase Analysis Light Scattering (PALS). The CNFs were produced through mechanical fibrillation of the pulp fibers in a SuperMassColloider (Model: MKZA6-2, Disk Model: MKGA6-80#, Masuko Sangyo Co., Ltd, Japan). Fibrillation was conducted at 2% solids loading for 5 h with a disk gap setting of −100 μm as described previously.[14] The surface charge of the CNFs was minimal. The mean sizes and crystallinities (CrI) of the CNFs and CNCs were measured previously as follows: 20 ± 14 nm (diameter) and 1030 ± 334 nm (length), 64.4% (CrI) for the CNFs; 19 ± 5 nm (diameter) and 151 ± 39 nm (length), 81.0% (CrI) for the CNCs.[53,54] Both types of nanofiber were provided in the form of aqueous suspensions and were used as received (concentration: CNCs = 5.7 wt%, CNFs = 1.8 wt%). Micro-sized cellulose fibers were obtained from commercial filter paper (Whatman International Ltd., grade 4, diameter 32 cm) by dispersing it in water using a food blender. Polyvinylpyrrolidone (PVP, M_w = 1 300 000), ethylene glycol (EG), sodium chloride (NaCl), silver nitrate ($AgNO_3$) and ammonium hydroxide (NH_4OH) were used to synthesize the silver nanowires (AgNWs). All chemicals were purchased from Sigma-Aldrich.

2.2. Fabrication of CNP

CNFs and CNCs with predetermined weight ratios (Table 1) were mixed by an ultrasonic processor (Cole-Parmer) for 5 min (250 W, room temperature). The solid content of the CNF/CNC mixtures was kept constant at 0.2 wt% in all formulations. The

Table 1 Optical properties of the CNP and the "micropaper"

CNF : CNC ratio	CNC content (wt%)	$R_{diffuse}$ at 600 nm (%)	T_{direct} at 600 nm (%)	T_{total} at 600 nm (%)	Haze (%)
10 : 0	0	10.9	31.1 ± 0.5	81.8	62.0
10 : 2	16.7	13.5	36.6 ± 0.2	82.4	55.6
10 : 6	37.5	9.5	61.6 ± 0.2	79.3	22.3
10 : 10	50.0	8.9	65.2 ± 0.3	83.8	22.1
6 : 10	62.5	7.4	72.5 ± 0.7	83.7	13.5
2 : 10	83.3	6.0	75.1 ± 0.4	83.4	10.0
0 : 10	100.0	5.2	74.2 ± 0.5	86.4	14.1
"Micropaper"		56.0	2.8 ± 0.4	32.8	91.4

mixtures were then filtered using a polyethylene filter (30 μm pore size) to remove remaining nanofiber aggregates. Wet CNP was produced using vacuum assisted filtration, a typical nanopaper-making technique.[55] Briefly, the mixtures were first vacuum-filtered using Anopore membranes (0.02 μm pore size, Whatman International Ltd) in a Wheaton funnel. The obtained wet nanopaper was then removed from the funnel and sandwiched between two membranes under pressure (about 0.36 kPa) and dried in a vacuum oven at 130 °C for 30 min. For comparison, "micropaper" was also fabricated following exactly the same procedure using the micro-sized cellulose fibers obtained from the Whatman filter paper.

We recognize that the CNF/CNC ratio in the produced CNP may be slightly different from the initial ratio selected for mixing because some nanofibers could go through the 20 nm pores in the filter (it might be more difficult for CNFs to do so because of their much larger length and their bundles/networks). However, we believe the chance for this to happen is small because the nanofibers need to be vertical to the filter to go through the pores. Moreover, if two fibers approach the same pore at the same time, the pore is blocked and no fibers can pass through. Therefore, throughout this paper we still use the initial CNF/CNC ratio to identify the produced CNP.

2.3. Synthesis of AgNWs

0.334 g PVP powder was completely dissolved in 25 mL EG by mild stirring at 170 °C for ~30 min. A NaCl solution in EG (50 μL, 0.43 M) and an $AgNO_3$ solution in EG (50 μL, 0.43 M) were simultaneously injected into the PVP solution and the mixture was stirred for 15 min to grow silver nanoparticle seeds. Another $AgNO_3$ solution in EG (10 mL, 0.12 M) was added dropwise for 12 min while stirring. The mixture was stirred for an additional 4 min. The reaction mixture was then cooled to room temperature (~ 50 °C h^{-1}) and ~100 mL water was added to stop the reaction. To remove the impurities, 2 mL aqueous NH_4OH was added to the mixture to dissolve the residual silver chloride (AgCl) generated during the reaction. AgNWs were imaged by a scanning electron microscope (SEM, Quanta 600 from FEI Company) and a transmission electron microscope (TEM, Titan G2 80-300 CT from FEI Company) to obtain their average diameters and lengths (Fig. S1†). The concentration of the as-prepared AgNW suspension was measured to be 0.028 wt%.

2.4. Fabrication of transparent CNP electrode

The process to fabricate transparent AgNW/CNP electrodes was similar to that of producing CNP. We first prepared five new AgNW suspensions by diluting 0.1, 0.5, 1, 2, and 3 g of the as-synthesized AgNW suspension in 20 g water. Then wet CNP was produced using vacuum-assisted filtration. With the wet CNP intact in the funnel, one of the new AgNW suspensions was added into the funnel and the filtration process continued until no liquid was left in the funnel. The obtained AgNW/CNP bilayer structure was dried using the method described in section 2.2 to eventually produce a transparent CNP electrode. AgNW areal density (mg m^{-2}) on the CNP was calculated based on the concentration and volume of the added AgNW suspensions.

2.5. LED demonstration using AgNWs/CNP electrode

A patterned AgNW layer was deposited on the surface of CNP by placing a polyvinylidene fluoride (PVDF) mask on the wet nanopaper before filtering the AgNW suspension. A commercially available aluminum gallium indium phosphide (AlGaInP)-based red LED (from Luwa System Inc.) was embedded between two patterned CNP electrodes to produce CNP-based LED devices. The electronic characteristics of the devices were measured using a customized light–current–voltage (*L–I–V*) testing system comprising a Keithley 2400 source meter, a Newport 2936C optical power meter and an Ocean optics 65000+ spectrometer.

2.6. Characterizations

Nanostructures of the prepared CNP, AgNWs and AgNWs/CNP electrodes were studied using a SEM (Quanta 600) operating at 5 or 10 kV and a TEM (Titan G2 80-300 CT) operating at 300 kV. Optical properties of the CNP and AgNWs/CNP electrodes were measured using a UV-VIS-NIR (UV-3600) spectrophotometer equipped with an ISR-3100 integrating sphere from Shimadzu Company. Transmittance of the samples was measured between 200–1200 nm wavelengths. The average values with standard deviations were calculated based on three measurements. All the digital photos in this study were taken by a consumer digital camera without using any polarizer and filter.

Sheet resistances (R_s) of the AgNW/CNP electrodes were measured using a CMT-SR2000N four-probe system (probe space 1 mm) from Materials Development Corporation. Measurements were taken at 10 different locations of each sample and the average value along with standard deviation was reported. To evaluate the stability of the electrical performance of the electrodes under deformation, the electrical resistance was measured *in situ* during a cyclic folding test on a 4 mm × 10 mm electrode. Two copper wires (15 cm long and 0.004 inch in diameter; C510 alloy, United Wire Technologies Inc.) were soldered onto the electrode using silver epoxy (Circuitworks CW2400 from ITW Chemtronics). A schematic illustration of the specimen was shown later in the Results and Discussion (Fig. 7A). The electrical resistance was measured by an Agilent U1252B multimeter, and the data were recorded by a computer. The folding action on the electrodes was provided

by an Instron 5944. The electrodes were also subjected to *in situ* resistance measurement under cyclic tension using the same Instron tester (5 N load cell). At least ten rectangular specimens (4 mm × 16 mm) were measured for each CNP.

Atomic force microscopy (AFM, Asylum MFP-3D) was employed to acquire height and phase images of the nanopaper surfaces. Probes (FESP from Bruker) with a spring constant of 2.8 N m^{-1} were used under the tapping mode. Average root mean square roughness (R_{RMS}) was obtained based on AFM scanning on three different areas of the nanopaper. R_{RMS} of the surfaces was calculated using Gwyddion software. Porosity and bulk density of the samples were measured using a Micromeritics AutoPore IV mercury porosimeter. The measurements were performed between 0.1 and 45 kPa after outgassing the sample for 2 hours at ambient temperature, and the data were analyzed using AutoPore IV 9500 (version 1.09) software. From the bulk density ρ_b and the skeletal density ρ_s, the overall porosity, Φ (dimensionless), and the specific pore volume, V_P (cm^3 g^{-1}), of the materials could be calculated as:

$$\Phi = 1 - \frac{\rho_b}{\rho_s} \quad (1)$$

$$V_P = \frac{1}{\rho_b} - \frac{1}{\rho_s} \quad (2)$$

3. Results and discussion

3.1. Optical properties of CNP

Fig. 1A compares the visual appearance of the aqueous suspensions of CNFs, CNCs and their mixtures. The micro-sized cellulose fibers isolated from Whatman filter paper were also dispersed in water at the same concentration for comparison. Due to their large diameter and length (diameter ≥ 30 μm; length ≥ 1000 μm), the micro-sized fibers precipitated quickly in water after the stirring was stopped (#1 in Fig. 1A).[49] By contrast, CNFs and CNCs both formed stable dispersions in water, with the former being translucent (#2) and the latter transparent (#8). The difference in transparency can be attributed to the presence of relatively large CNF bundles and networks[54] in the CNF suspension that scattered more light than the individually dispersed CNCs in the CNC suspension. The CNF bundles were formed through hydrogen bonding between the –OH groups on the fiber surface, and the networks were caused by physical entanglement between the fibers. By contrast, most CNCs in the suspension remained individually dispersed due to electrostatic repulsion originating from the sulfate ($-OSO_3^-$) groups on the fiber surfaces.[56] The transparency of the mixed CNC/CNF suspensions increased with increasing CNC content (#3 through #7). This could be attributed to the fact that CNFs at lower concentrations exhibit weaker tendency to bundle and network. In addition, the

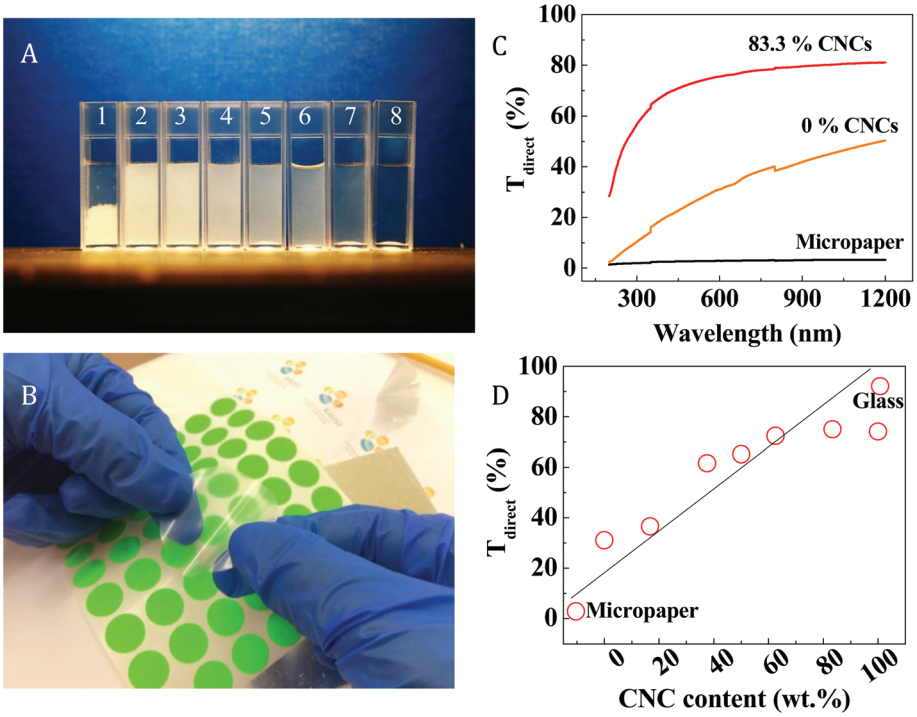

Fig. 1 Optical images of various fiber suspensions (under natural light) and their direct transmittance as hybrid nanopapers; (A) from left to right, #1: suspension of the micron-sized cellulose fibers; #2 to #8: mixed CNF/CNC suspensions with 0%, 16.7%, 37.5%, 50.0%, 62.5%, 83.3% and 100.0% of CNCs. The solid content of all the suspensions was 0.2 wt%. Suspensions #2 to #8 are stable for at least 24 hours. (B) Visual appearance of a piece of hybrid CNP (62.5% CNCs); (C) direct transmittance of the "micropaper", all-CNF CNP, and the hybrid CNP (83.3% CNCs); (D) Direct transmittance as a function of the CNC content at 600 nm wavelength.

added CNCs could also act as "spacers" to reduce the contacts between the CNFs and therefore hinder the CNF bundling and networking processes.

The transparency of the hybrid CNP follows the same trend, *i.e.*, the transparency increases with the increasing CNC content. Fig. 1B shows the visual appearance of a piece of highly transparent hybrid CNP (62.5% CNCs). T_{direct} was measured between 200–1200 nm wavelength for quantification of the optical properties. Fig. 1C compares the T_{direct} of two CNP samples (0% CNCs and 83.3% CNCs, respectively) and one "micropaper" sample. Across the entire wavelength range, the "micropaper" exhibits the lowest T_{direct} (≈ 0); T_{direct} of the all-CNF CNP increases significantly and it further improves for the hybrid CNP. For instance, at 600 nm, T_{direct} for the "micropaper", all-CNF CNP, and the hybrid CNP are 2.8%, 31.1% and 75.1%, respectively. The dependence of T_{direct} on the CNC content is shown in Fig. 1D and Table 1, which indicate that the transmittance increases with the increasing CNC content initially and tends to level off after the content exceeds 62.5%. The plateau value of T_{direct} (~75%) exceed most reported values for CNF-based CNP;[46] it also approaches that of poly (ethylene terephthalate) (PET, >85%),[57] ITO glass (85%)[58] and pure silicon oxide glass (92%). This high T_{direct} is attributed to the reduced surface roughness, porosity and internal pore size of the CNP after the addition of CNCs, as will be discussed below.

We calculated the haze (H_T) of the CNP to further study its optical properties. H_T is defined as:[59,60]

$$H_T = \frac{T_{diffuse}}{T_{total}} \times 100\% \quad (3)$$

where $T_{diffuse}$ is the amount of forward-scattered light (light scattered more than 2.5° from the incident light). A higher H_T suggests that a larger portion of the transmitted light is scattered (diffused), lowering the in-line transmission and causing the sample to be translucent and milky (Fig. 2A inset). The all-CNF CNP in this study has a H_T of 62.0%, which is similar to the values reported in other studies.[31] At this level, the CNP exhibits obvious haze as shown by the blurred printing that is located 1 cm below the CNP sample (Fig. 2B). By contrast, the haze is greatly reduced in the hybrid CNP to 10.0%, creating a much clearer printing at the same distance. The general trend of H_T as a function of the CNC content is presented in Fig. 2A, which shows that the H_T of the CNP with high CNC contents (*i.e.*, 62.5 wt% and 83.3 wt%) approaches that of transparent plastic film, glass and ITO glass (Fig. 2A and Table S1† [61–69]),

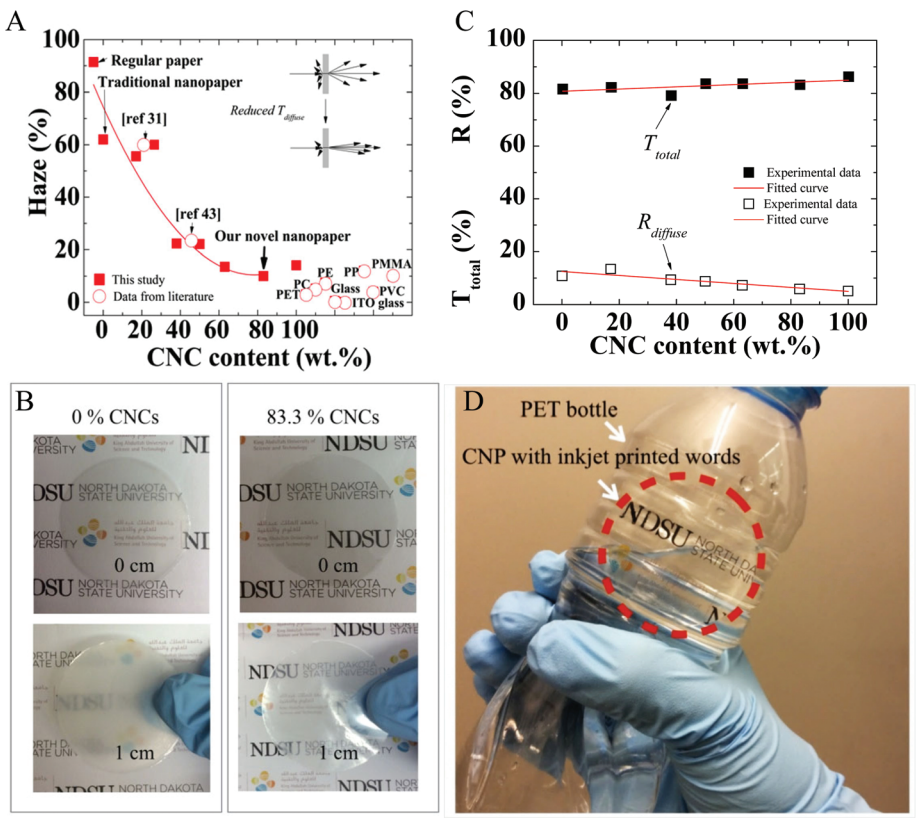

Fig. 2 Optical properties of the CNF/CNC hybrid CNP with different CNC contents. (A) Haze of the hybrid CNP as a function of the CNC content. Haze of the CNP made by other researchers and of other transparent substrates are shown for comparison.[61–69] (B) Visual comparison of the all-CNF CNP and the hybrid CNP (83.3 wt% CNCs) to show the haze effect. The "cm" designations indicate the distances between the CNP and the underneath printing. (C) Total transmittance and diffuse reflection as a function of the CNC content. (D) A piece of transparent CNP (83.3 wt% CNCs) with inkjet-printed words was pasted on a PET bottle.

suggesting the potential of the hybrid CNP to replace these traditional transparent materials.

While the haze of a material is mostly affected by transmission of light, the gloss of the material depends on how light is reflected on the material surface. To distinguish between haze and gloss, we also measured the diffuse reflection ($R_{diffuse}$) of all CNP (Table 1). $R_{diffuse}$ is caused by the surface roughness and inhomogeneity of the material. A material with low $R_{diffuse}$ exhibits high gloss. Fig. 2B shows that $R_{diffuse}$ decreases with increasing CNC content, indicating improved surface roughness and overall material homogeneity. In general, a combination of high T_{direct}, high T_{total}, low $R_{diffuse}$ and low H_T renders CNP the quality of high-transparency, high-gloss, and low-haze, which is demonstrated by the CNP in Fig. 2C. In this digital photo, a piece of circular CNP, on which "NDSU" and other words are printed using a commercial inkjet printer, is pasted on the surface of a PET bottle. The photo shows negligible visual difference between the CNP and the plastic, suggesting the possibility to replace the plastic with the CNP in some applications.

The results and discussion about T_{direct}, $T_{diffuse}$, H_T and $R_{diffuse}$ of the CNP show that the optical properties of the hybrid CNP can be tailored by simply adjusting the ratio between CNFs and CNCs. This facile method allows low-cost, mass production of CNP that meets the optical requirements of various applications. Although the vacuum filtration process can take up to 8 hours to complete, the process can be scaled up by performing filtration on large filter surfaces and so large areas of nanopaper can be produced in one batch. It is also worth noting that no birefringence was observed on the CNP. This could be attributed to random orientation of the cellulose nanofibers, which rendered the CNP isotropic.

3.2. Mechanism for high transparency and low haze

The transparency and haze of CNP is related to its surface roughness and porosity.[70,71] The surfaces of the "micropaper", all-CNF CNP and the hybrid CNP (83.3% CNCs) are compared in Fig. 3, which qualitatively demonstrates the increasing surface smoothness and decreasing porosity of the three samples. The surface roughness of all CNP samples was further measured using AFM (Fig. 4A). The surface profiles of the all-CNF and the hybrid CNP are compared in Fig. 4B, which shows that the latter has a much smaller maximum valley depth (R_v). The surface roughness of the hybrid CNP over a 1 μm line is 1.21 nm with a R_v of 4.71 nm. These values are comparable to those of transparent nanopaper derived from TEMPO-preoxidized and microfluidized cellulose nanofibrils.[13] The surface roughness over a 1 × 1 μm^2 area (R_{RMS}) was also calculated for all CNP and the results are plotted as a function of CNC content in Fig. 4C. The curve shows an approximately linear decrease in R_{RMS} with the increasing CNC content, confirming the visual observations in Fig. 3. R_{RMS} decreases from 22.11 nm for the all-CNF CNP to 5.75 nm for the all-CNC CNP.

Similar to the decreasing R_{RMS}, the porosity Φ of the CNP also decrease with the increasing CNC content (Fig. 4D). Φ decreases approximately linearly from 13.3% to 7.5% as the CNC content increases from 0% to 100%. The trends of the R_{RMS} and porosity both indicate that the surface of CNP becomes smoother because voids are gradually filled with the addition of CNCs. Moreover, the bulk density of CNP measured by mercury porosimetry increases from *ca.* 1.3 to 1.5 g cm^{-3} when the CNC content increases from 0% to 100% (Fig. 4D, noting that the density of crystalline cellulose is 1.5–1.6 g cm^{-3}),[72] confirming the decreasing porosity of the nanopaper with higher CNC content. As a comparison, the "micropaper" shows a porosity of 80.6% and a bulk density of ~0.3 g cm^{-3}. The huge differences in porosity and density between the "micropaper" and the nanopaper are due to their different fiber sizes and micro/nano structures, which result in different optical properties as shown above.

High surface roughness and porosity lead to high diffusive scattering and therefore low direct transmittance and high haze. The transparency of CNP increases mainly through the reductions in its surface roughness, porosity and pore size. To achieve such reduction, oil and polymers (*e.g.*, polyvinyl alcohol, polyethelyene oxide and epoxy) have been used to fill the voids between CNFs and their bundles in CNP;[53,73,74] CNP has been laminated with thermoplastics to fill the voids;[46] cellulose nanofibers have also been refined by TEMPO oxidation with assistance of fluidization to reduce fiber diameters and hence the size of the voids.[13,30,31,37,42,75] Here, we use CNCs as

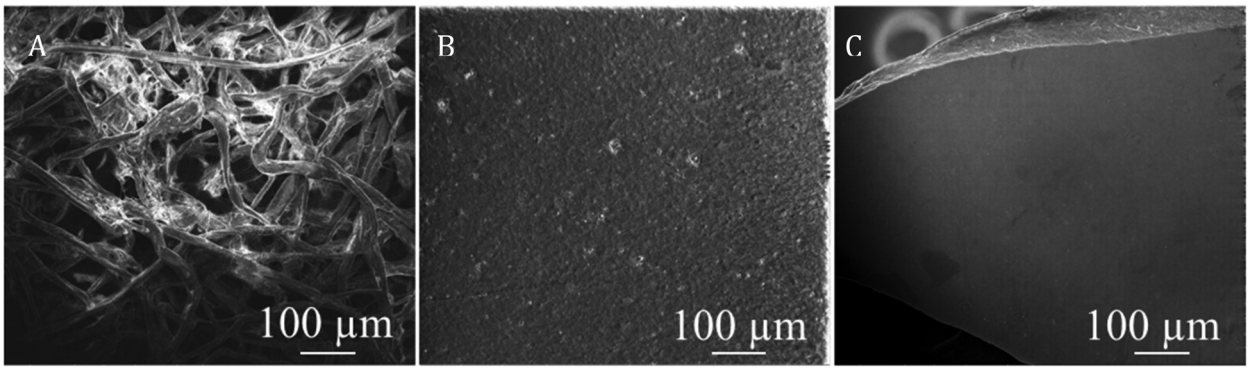

Fig. 3 SEM images of the paper. (A) "Micropaper"; (B) all-CNF CNP; (C) hybrid CNP (83.3% CNCs).

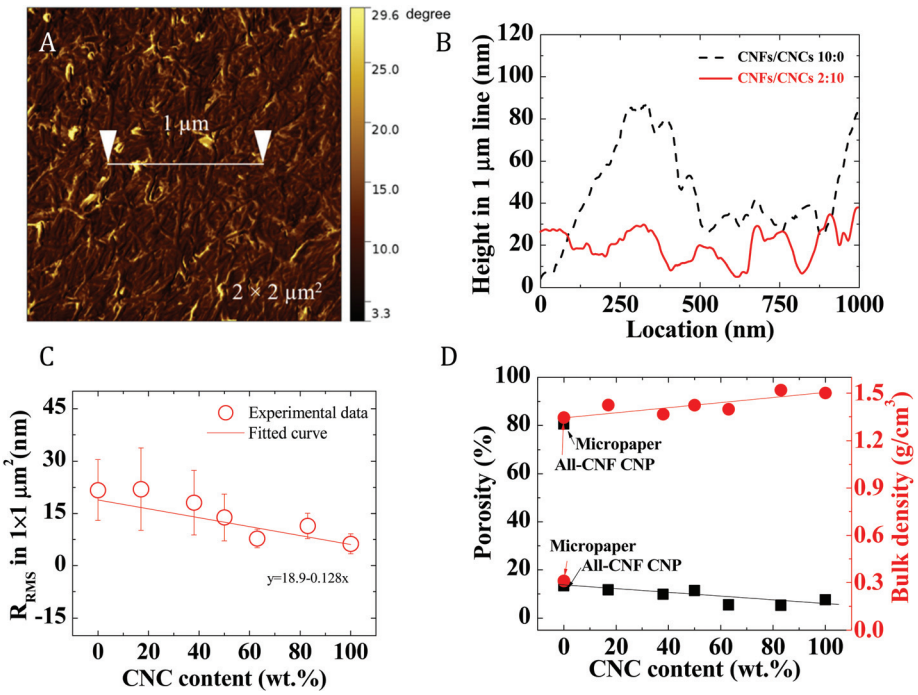

Fig. 4 Surface morphology and microstructure of the hybrid CNP containing different content of CNCs. (A) AFM phase image of a hybrid CNP sample (83.3 wt% CNCs); (B) comparison of the surface profiles between the all-CNF CNP and the hybrid CNP over 1 μm length; (C) R_{RMS} as a function of CNC content. The error bars represent standard deviation based on three measurements. (D) Porosity and bulk (apparent) density of CNP as a function of CNC content.

a "nanofiller" to fill the voids in the CNF network and to smoothen the surfaces of the resultant hybrid CNP. This method is unique as no petroleum-based components are needed and the product exhibits comparable or superior optical performance compared with previous materials.

The effect of the pores on light transmission in the nanopaper can be understood using the following equation:[76]

$$\mathrm{RIT} = (1 - R)\cdot\exp(-\gamma_{\mathrm{pore}}\cdot t) \quad (4)$$

where RIT, γ_{pore} and t are the real in-line transmission (which is close to T_{direct} measured in this study), the scattering coefficient for the pores and the sample thickness, respectively. R is the reflection loss (the Fresnel reflection coefficient) on the sample's surface and can be calculated using:

$$R = \frac{2R'}{1+R'} \quad R' = \left(\frac{n-1}{n+1}\right)^2 \quad (5)$$

where n is the refractive index of cellulose (n = 1.4701).[77,78] The loss in transmission caused by absorption, scattering on the sample's surface and scattering on the CNC/CNF interfaces is neglected in eqn (4). The omission of the surface scattering is justified by the low surface roughness of the hybrid CNP, and the omission of the CNC/CNF interface scattering is because CNCs and CNFs have very similar refractive indexes. Light scattering by the pores is considered the main factor in this equation.

Eqn (4) shows that RIT (*i.e.*, T_{direct} in this study) decreases with increasing γ_{pore}. From the measured T_{direct} and t (Table 1), γ_{pore} of the CNP with different CNC contents can be calculated and the results are shown in Fig. 5A. The curve demonstrates a decreasing trend of γ_{pore} due to the progressive filling by the CNCs. For spherical pores with a radius of a, γ_{pore} can be calculated by:[79]

$$\gamma_{\mathrm{pore}} = NC_{\mathrm{sca}} = NQ_{\mathrm{sca}}\pi a^2 = \frac{3V_{\mathrm{pore}}}{4a}Q_{\mathrm{sca}} \quad (6)$$

where N is the number of pores, C_{sca} is the scattering cross section, V_{pore} is the porosity, and Q_{sca} is the scattering efficiency factor that can be calculated using the Mie theory. Eqn (6) clearly shows that a decrease in V_{pore} will lead to a decrease in γ_{pore}, which agrees with our results (Fig. 5B). On the other hand, the effect of the pore radius, a, on γ_{pore} is more complicated because Q_{sca} varies with the radius. It has been shown that Q_{sca} reaches the maximum value when a equals 0.6–0.7 of the incident wavelength (600 nm in this case).[80] Below this size, Q_{sca}/a is close to a constant. The pore radius of the CNP is estimated to be lower than this critical value based on the AFM surface profile (Fig. 4B). We therefore conclude that the reduction in V_{pore} is the primary reason for the nanopaper's high direct transmission and low haze.

It should be pointed out that in this study all the CNP and the "micropaper" were prepared with equal mass. Undergoing the same vacuum filtration and pressing procedure, the variation of the thickness of the obtained hybrid CNP and all-CNF CNP was within ±1.5 μm with an average thickness of ~15 μm. This thickness variation was due to different degrees of nano-

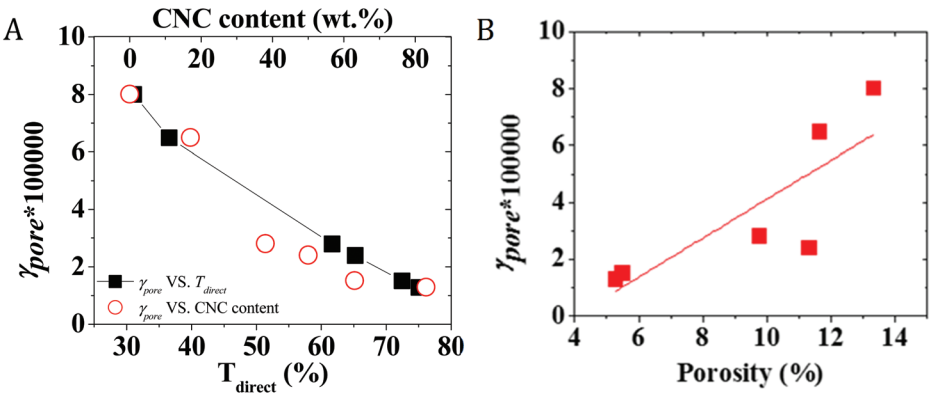

Fig. 5 Optical parameters in different CNF/CNC hybrid nanopapers. (A) Scattering coefficient, γ_{pore}, as a function of T_{direct} and CNC concentration; (B) dependence of γ_{pore} on the porosity of the nanopaper.

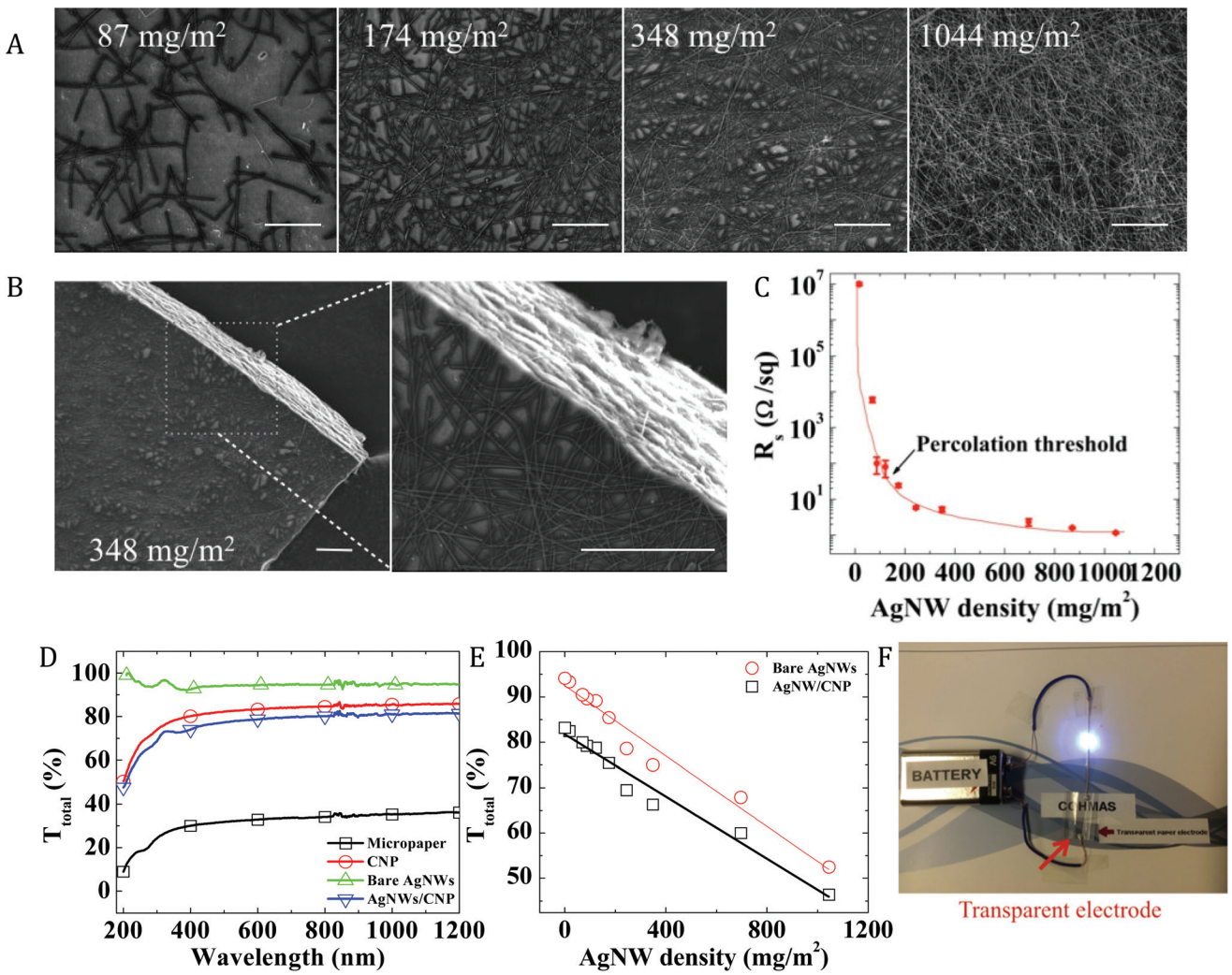

Fig. 6 Morphology, electrical and optical properties of various AgNW/CNP electrodes. (A) SEM images showing AgNWs deposited on a CNP substrate at different areal densities; (B) SEM images of the cross-section of the electrode; (C) sheet resistance as a function of AgNW areal density; (D) T_{total} as a function of wavelength for the "micropaper", CNP (83.3 wt% CNCs), bare AgNW network (calculated using T_{total} of bare AgNWs $= \frac{T_{total}\text{ of AgNWs/CNP}}{T_{total}\text{ of CNP}}$) and the AgNW/CNP electrode (121 mg m^{-2}, 83.3 wt% CNCs); (E) T_{total} as a function of AgNW areal density in the bare AgNWs and the AgNW/CNP electrode; (F) demonstration of the function of the transparent AgNWs/CNP electrode using a series circuit composed of a battery, a 2 × 3 cm^2 AgNW/CNP electrode (121 mg m^{-2}, 83.3 wt% CNCs) and an LED lamp. Scale bars in the SEM images are 20 μm.

Table 2 Electrical and optical properties of the bare AgNW network and the AgNWs/CNP electrodes. T_{total} is sampled at 600 nm wavelength, T_{total} of the CNP substrate is 83.4%. The numbers in parenthesis are standard deviations based on ten measurements

AgNW areal density (mg m^{-2})	R_s of AgNWs/CNP (Ω sq^{-1})	T_{total} of bare AgNWs (%)	T_{total} of AgNWs/CNP (%)
1044	1.16 (0.07)	52.5	46.4
696	2.33 (0.54)	67.9	60.0
348	5.22 (0.82)	75.0	66.3
243	5.82 (0.46)	78.7	70.0
174	23.48 (2.57)	85.4	75.5
121	75.48 (40.07)	89.2	78.8
87	104.33 (49.55)	89.6	79.2
69	6.33 (1.33) (kΩ sq^{-1})	90.5	80.0
17	10.23 (0.96) (MΩ sq^{-1})	93.4	82.5

fiber packing between the samples (which resulted in different porosities) and unevenness in thickness of each individual CNP. Therefore the porosity of CNP was a more accurate and reliable parameter than its thickness to be used in the discussion of the optical properties. The contribution of the thickness was also inherently taken into account through the use of the porosity because these two parameters were related. As an example, the thickness of the "micropaper" was about 10 times that of the CNP because of its poor packing/high porosity, which led to its low optical properties.

3.3. Sheet resistance and transmittance of AgNW/CNP electrodes

The conductive AgNW network deposited on the CNP substrate (83.3% CNCs) is shown in Fig. 6A and B. The areal density of the nanowire network, defined as the weight of AgNWs per unit substrate area, increases from 87.0 to 1044.5 mg m^{-2}, resulting in an increasingly dense AgNW network as shown in the figure. The AgNWs have an average diameter of 74 nm and an average length of 37.5 μm, yielding an aspect ratio of 506. This high aspect ratio can lead to a percolated AgNW network at a low areal density.[81] As shown in Fig. 6C, the sheet resistance, R_s of the electrodes initially decreases rapidly with increasing AgNW density and then stabilizes when the AgNW density is high, suggesting a percolation threshold of 121 mg m^{-2} (data in Table 2). The R_s values (1.16–23.48 Ω sq^{-1}) for the AgNW/CNP electrodes with percolated AgNWs are lower than or comparable to the value (16 Ω sq^{-1}) for AgNW/glass electrodes with a transmittance of 86% reported in a prior study.[82]

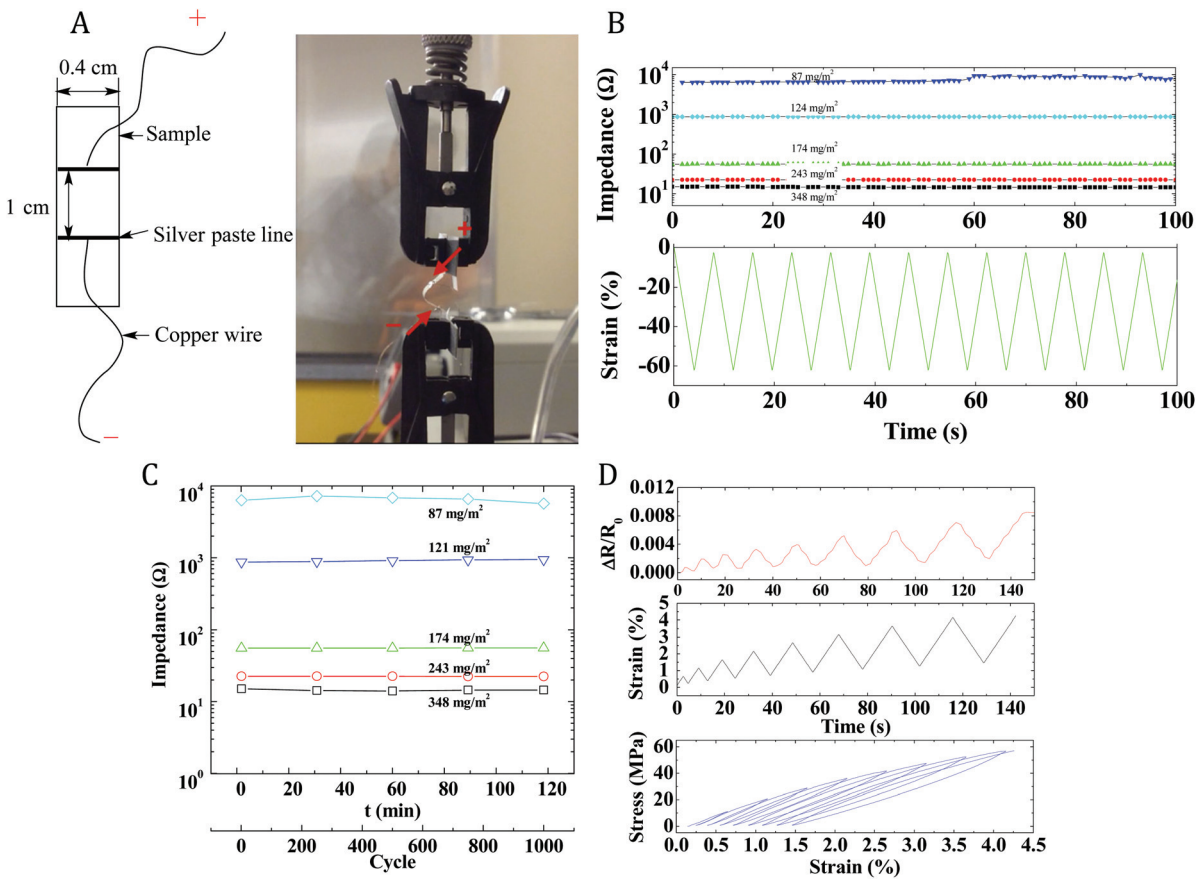

Fig. 7 Damage-tolerant electrical conductivity of the AgNWs/CNP electrodes. (A) Illustration of *in situ* electrical resistance measurement of the electrodes under cyclic folding and tension; (B) resistance of the electrodes with different AgNW areal densities during the first 12 folding cycles; (C) resistance of the electrodes through 1000 folding cycles; (D) resistance of a representative electrode (348 mg m^{-2} AgNW density) under increasing cyclic tensile strain.

The total transmittance (T_{total}) of the AgNW/CNP electrode is compared with that of a bare AgNW network (*i.e.* as an individual layer) in Fig. 6D and Table 2. The transmittance of the AgNW network can be calculated using the equation in Fig. 6 after the transmittance of the CNP substrate and the bilayer electrode are measured. The bare AgNW network is found to be more transparent than the CNP. Depositing the highly transparent AgNW network on the CNP substrate only slightly decreases the T_{total} of the CNP. As a control, the T_{total} of the "micropaper" is much lower than those of the three samples. As expected, the transmittance decreases with increasing AgNW areal density in both the electrode and the AgNW network (Fig. 6E). The fact that the two linear fitting lines in the figure are parallel suggests that the decrease is primarily due to the increasing AgNW areal density and the downshift of the top line (for the bare AgNWs) is caused by the CNP substrate. Fig. 6F demonstrates the high conductivity of the AgNW/CNP electrode by using it to connect a circuit and light an LED.

3.4. Damage-tolerant electrical conductivity of AgNWs/CNP electrodes

The electrical resistance of the electrode was monitored under cyclic folding between two grips (Fig. 7A). The folding action was performed by changing the distance between the grips, and the degree of folding was quantified by a strain that is defined as the ratio of the travel distance of one of the grips to the initial gap distance between the two grips. Fig. 7B and C show the resistance of the electrodes with different AgNW areal densities under the cyclic strain. It is clear that the resistance decreases with increasing areal density and that the resistance remains nearly constant despite the folding action (Fig. 7B). All the samples maintain consistent resistance after 1000 folding cycles (Fig. 7C). These results demonstrate the robustness of the electrodes under the folding action, which can be attributed to the strong adhesion between the AgNW network and the CNP substrate and between the individual AgNWs at their junctions.

The resistance of the electrode was also measured while the sample was under increasing cyclic tensile strain (until the sample fractured at ~4% strain). A comparison of the resistance and the strain curves in Fig. 7D shows that the former traces the latter, suggesting a linear relationship between the strain and the resistance change. When a tensile strain is exerted on the electrode, the nanowires can elongate and/or some connections between the nanowires can be broken, both of which increase the resistance. However, the reversibility of the resistance under cyclic strain indicates that the deformation/breakage is transient. The linear strain-resistance relationship suggests the electrode's potential as a strain sensor.[6,83,84]

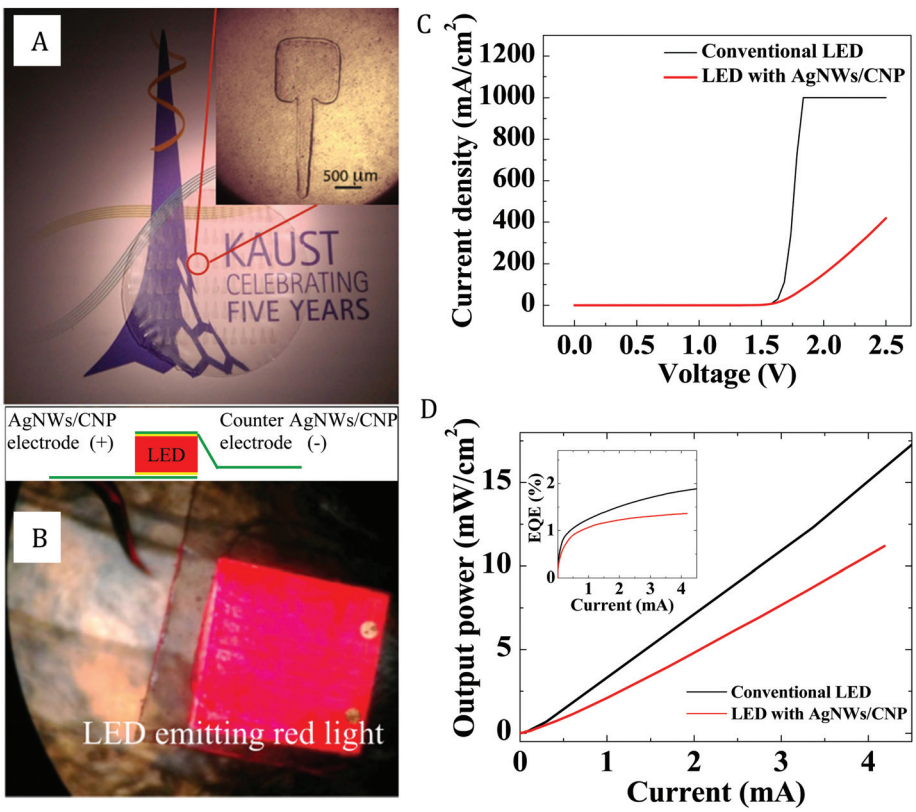

Fig. 8 Demonstration of the AgNWs/CNP electrodes in a LED assembly. (A) Photo of the patterned leads made using the electrode; (B) photo showing red light emitted from the LED sandwiched between two AgNW/CNP leads. The inset shows the diagram of the device; (C) *J*–*V* characteristics of the LEDs with the AgNW/CNP and the conventional leads. (D) *L*–*I* and EQE–*I* curves for the two LEDs.

3.5. AgNWs/CNP electrodes for LED devices

The transparent AgNW/CNP electrodes developed in this study can be used to build flexible display devices. As a first demonstration, we produced "screw"-like, micro-sized AgNW/CNP leads formed by patterning the AgNW layer on a CNP substrate containing 83.3 wt% CNCs (Fig. 8A). We then sandwiched an AlGaInP-based red LED microchip between two of the transparent leads (Fig. 8C inset). Red light was emitted when a direct-current (DC) voltage was applied on the two leads (Fig. 8B). The current density–voltage (*J–V*) characteristic of the device was measured and compared with that of a LED device using conventional Ti/Au metallic leads (Fig. 8C). The comparison indicates that the turn-on voltage of the LED with the AgNW/CNP leads is similar to that of the conventional lead. The lower current density for the AgNW/CNP leads may be due to the contact resistance at the AgNW junctions, which is expected to be reduced using methods such as localized annealing. Fig. 8D shows the light output power–current (*L–I*) and external quantum efficiency–current (*EQE–I*) relations of our and the conventional LEDs. Both the output power and EQE of our LED are moderately lower than those of the conventional LED, likely due to its higher contact resistance. Nevertheless, using AgNW/CNP as transparent electrodes in LEDs is feasible. Multiple light emitting devices can be packed on the patterned AgNW/CNP electrodes and flexible display devices can then be produced. This demonstration paves the way for further development of flexible displays based on our facile nanopaper fabrication technology.

4. Conclusion and outlook

In this study, we developed a facile methodology to synthesize highly transparent, mechanically robust, hybrid CNP consisting of CNFs and CNCs. In this CNP, CNFs form an entangled network to impart the nanopaper strength and flexibility; CNCs act as a rigid nanofiller to modify its structure and properties. Optical properties of the nanopaper can be tailored by varying the ratio between CNFs and CNCs. The concentration of CNCs affects the surface roughness, porosity and CNF entanglement of the nanopaper, resulting in varied optical properties. Our hybrid CNP has equivalent or higher total transmittance and much smaller haze compared with the all-CNF CNP reported in the literature. This is due to the low surface roughness and porosity of the hybrid CNP that are rendered by the "filling" effect of CNCs. Depositing AgNWs on a hybrid CNP substrate produces transparent, flexible electrodes, whose conductivity is dependent on the areal density of AgNWs. *In situ* measurement of the conductivity during cyclic loading shows that the electrical property of the electrode is tolerant to damage under folding deformation. Under tensile deformation, the electrical resistance of the electrode exhibits a linear relationship with the tensile strain, suggesting its potential to be used as a strain sensor. A proof-of-concept LED device has been created to demonstrate the nanopaper electrode's potential use in flexible electronic devices. Further work to decrease the contact resistance of the electrode for use in large area flexible displays will be conducted.

We have achieved a high direct transmittance of 75.1% and a low haze of 10.0% in our nanopaper. With ongoing intensive studies on nanopaper, these values will almost certainly be surpassed in the future. These values, however, indicate that nanopaper can already be used in flexible devices to replace traditional plastics (*e.g.*, PET). Even more importantly, we have demonstrated a facile method that produces nanopaper with a wide range of optical and electrical properties, which should make production of the material appealing.

Due to the hydrophilic nature of cellulose, ensuring the structural integrity and performance stability of the CNP-based electrodes in humid environment can be challenging. One solution is to develop hydrophobic or even superhydrophobic CNP by surface engineering of the CNP (*e.g.* creating a hierarchical surface structure and applying hydrophobic nanoparticles on the surface at the same time). Through the tensile tests we have also found that the tensile properties of the hybrid CNP strongly depends on the CNF/CNC ratio. This is understandable because CNCs and CNFs exhibit different mechanical properties and the structure (*e.g.* porosity) of the CNP varies with the ratio. While the CNP generally showed a low strain-at-failure under tension, it was quite flexible and damage-tolerant as demonstrated by the folding tests. The focus of this study is on optical and electrical properties of the nanopaper, which are critical to the performance of flexible displays. The results about its mechanical properties will be reported in a future publication.

Acknowledgements

Financial supports from North Dakota EPSCoR, KAUST Baseline, and a USDA Agriculture and Food Research Initiative (AFRI) Competitive Grant (no. 2011-67009-20056) are greatly appreciated.

References

1 A. R. Madaria, A. Kumar and C. Zhou, *Nanotechnology*, 2011, **22**, 245201.
2 S. Reineke, F. Lindner, G. Schwartz, N. Seidler, K. Walzer, B. Lüssem and K. Leo, *Nature*, 2009, **459**, 234–238.
3 D.-S. Leem, A. Edwards, M. Faist, J. Nelson, D. D. C. Bradley and J. C. de Mello, *Adv. Mater.*, 2011, **23**, 4371–4375.
4 M. Nasr Saleh and G. Lubineau, *Sol. Energy Mater. Sol. Cells*, 2014, **130**, 199–207.
5 J. Zhou and G. Lubineau, *ACS Appl. Mater. Interfaces*, 2013, **5**, 6189–6200.
6 J. Zhou, T. Fukawa, H. Shirai and M. Kimura, *Macromol. Mater. Eng.*, 2010, **295**, 671–675.
7 L. Hu, H. S. Kim, J. Lee, P. Peumans and Y. Cui, *ACS Nano*, 2010, **4**, 2955–2963.

8 S. De, T. M. Higgins, P. E. Lyons, E. M. Doherty, P. N. Nirmalraj, W. J. Blau, J. J. Boland and J. N. Coleman, *ACS Nano*, 2009, **3**, 1767–1774.
9 X.-Y. Zeng, Q.-K. Zhang, R.-M. Yu and C.-Z. Lu, *Adv. Mater.*, 2010, **22**, 4484–4488.
10 J. Liang, L. Li, K. Tong, Z. Ren, W. Hu, X. Niu, Y. Chen and Q. Pei, *ACS Nano*, 2014, **8**, 1590–1600.
11 L. Hu, G. Zheng, J. Yao, N. Liu, B. Weil, M. Eskilsson, E. Karabulut, Z. Ruan, S. Fan, J. T. Bloking, M. D. McGehee, L. Wågberg and Y. Cui, *Energy Environ. Sci.*, 2013, **6**, 513.
12 F. Cherubini, *Energy Convers. Manage.*, 2010, **51**, 1412–1421.
13 J. Huang, H. Zhu, Y. Chen, C. Preston, K. Rohrbach, J. Cumings and L. Hu, *ACS Nano*, 2013, **7**, 2106–2113.
14 Q. Q. Wang, J. Y. Zhu, R. Gleisner, T. A. Kuster, U. Baxa and S. E. McNeil, *Cellulose*, 2012, **19**, 1631–1643.
15 J. Y. Zhu, R. Sabo and X. Luo, *Green Chem.*, 2011, **13**, 1339.
16 M. Henriksson, L. A. Berglund, P. Isaksson and T. Lindstro, *Biomacromolecules*, 2008, **9**, 1579–1585.
17 W. Wang, M. D. Mozuch, R. C. Sabo, P. Kersten, J. Y. Zhu and Y. Jin, *Cellulose*, 2015, **22**, 351–361.
18 H. Fukuzumi, T. Saito, T. Iwata, Y. Kumamoto and A. Isogai, *Biomacromolecules*, 2009, **10**, 162–165.
19 L. Wgberg, G. Decher, M. Norgren, T. Lindström, M. Ankerfors, K. Axnäs, L. Wagberg, G. Decher, M. Norgren, T. Lindstrom, M. Ankerfors and K. Axnas, *Langmuir*, 2008, **24**, 784–795.
20 Q. Wang, J. Y. Zhu and J. M. Considine, *ACS Appl. Mater. Interfaces*, 2013, **5**, 2527–2534.
21 L. Chen, Q. Wang, K. Hirth, C. Baez, U. P. Agarwal and J. Y. Zhu, *Cellulose*, 2015, 1753–1762.
22 M. Jonoobi, R. Oladi, Y. Davoudpour, K. Oksman, A. Dufresne, Y. Hamzeh and R. Davoodi, *Cellulose*, 2015, **22**, 935–969.
23 H. P. S. Abdul Khalil, Y. Davoudpour, M. N. Islam, A. Mustapha, K. Sudesh, R. Dungani and M. Jawaid, *Carbohydr. Polym.*, 2014, **99**, 649–665.
24 L. Chen, J. Y. Zhu, C. Baez, P. Kitin and T. Elder, *Green Chem.*, 2016, DOI: 10.1039/c6gc00687f.
25 M. S. Peresin, Y. Habibi, J. O. Zoppe, J. J. Pawlak and O. J. Rojas, *Biomacromolecules*, 2010, **11**, 674–681.
26 A. N. Nakagaito and H. Yano, *Cellulose*, 2008, **15**, 555–559.
27 M. S. Wang, F. Jiang, Y.-L. Hsieh and N. Nitin, *J. Mater. Chem. B*, 2014, **2**, 6226.
28 X. Xu, J. Zhou, D. H. Nagaraju, L. Jiang, V. R. Marinov, G. Lubineau, H. N. Alshareef and M. Oh, *Adv. Funct. Mater.*, 2015, **25**, 3193–3202.
29 H. Sehaqui, A. Liu, Q. Zhou and L. a. Berglund, *Biomacromolecules*, 2010, **11**, 2195–2198.
30 H. Zhu, S. Parvinian, C. Preston, O. Vaaland, Z. Ruan and L. Hu, *Nanoscale*, 2013, **5**, 3787–3792.
31 Z. Fang, H. Zhu, Y. Yuan, D. Ha, S. Zhu, C. Preston, Q. Chen, Y. Li, X. Han, S. Lee, G. Chen, T. Li, J. Munday, J. Huang and L. Hu, *Nano Lett.*, 2014, **14**, 765–773.
32 H. Sehaqui, N. E. Mushi, S. Morimune, M. Salajkova, T. Nishino and L. A. Berglund, *ACS Appl. Mater. Interfaces*, 2012, **4**, 1043–1049.
33 A. Walther, J. V. I. Timonen, I. Díez, A. Laukkanen and O. Ikkala, *Adv. Mater.*, 2011, **23**, 2924–2928.
34 S. J. Eichhorn, A. Dufresne, M. Aranguren, N. E. Marcovich, J. R. Capadona, S. J. Rowan, C. Weder, W. Thielemans, M. Roman, S. Renneckar, W. Gindl, S. Veigel, J. Keckes, H. Yano, K. Abe, M. Nogi, A. N. Nakagaito, A. Mangalam, J. Simonsen, A. S. Benight, A. Bismarck, L. a. Berglund and T. Peijs, *J. Mater. Sci.*, 2009, **45**, 1–33.
35 Z. Fang, H. Zhu, C. Preston, X. Han, Y. Li, S. Lee, X. Chai, G. Chen and L. Hu, *J. Mater. Chem. C*, 2013, **1**, 6191.
36 H. Tang, N. Butchosa and Q. Zhou, *Adv. Mater.*, 2015, **27**, 2070–2076.
37 H. Yano, J. Sugiyama, A. N. Nakagaito, M. Nogi, T. Matsuura, M. Hikita and K. Handa, *Adv. Mater.*, 2005, **17**, 153–155.
38 S. C. M. Fernandes, L. Oliveira, C. S. R. Freire, A. J. D. Silvestre, C. P. Neto, A. Gandini and J. Desbriéres, *Green Chem.*, 2009, **11**, 2023.
39 S. Iwamoto, A. N. Nakagaito, H. Yano and M. Nogi, *Appl. Phys. A*, 2005, **81**, 1109–1112.
40 X. Sun, Q. Wu, S. Ren and T. Lei, *Cellulose*, 2015, **22**, 1123–1133.
41 M.-C. Hsieh, C. Kim, M. Nogi and K. Suganuma, *Nanoscale*, 2013, **5**, 9289–9295.
42 Z. Fang, H. Zhu, W. Bao, C. Preston, Z. Liu, J. Dai, Y. Li and L. Hu, *Energy Environ. Sci.*, 2014, **7**, 3313–3319.
43 H. Zhu, Z. Fang, C. Preston, Y. Li and L. Hu, *Energy Environ. Sci.*, 2014, **7**, 269–287.
44 M. Nogi, N. Komoda, K. Otsuka and K. Suganuma, *Nanoscale*, 2013, **5**, 4395–4399.
45 M. Nogi and H. Yano, *Adv. Mater.*, 2008, **20**, 1849–1852.
46 M. Nogi, S. Iwamoto, A. N. Nakagaito and H. Yano, *Adv. Mater.*, 2009, **21**, 1595–1598.
47 H. Koga, M. Nogi, N. Komoda, T. T. Nge, T. Sugahara and K. Suganuma, *NPG Asia Mater.*, 2014, **6**, e93.
48 H. Zhu, Z. Xiao, D. Liu, Y. Li, N. J. Weadock, Z. Fang, J. Huang and L. Hu, *Energy Environ. Sci.*, 2013, **6**, 2105.
49 A. Isogai, T. Saito and H. Fukuzumi, *Nanoscale*, 2011, **3**, 71–85.
50 C. Preston, Z. Fang, J. Murray, H. Zhu, J. Dai, J. N. Munday and L. Hu, *J. Mater. Chem. C*, 2014, **2**, 1248.
51 H. Sehaqui, Q. Zhou, O. Ikkala and L. A. Berglund, *Biomacromolecules*, 2011, **12**, 3638–3644.
52 Q. Q. Wang, J. Y. Zhu, R. S. Reiner, S. P. Verrill, U. Baxa and S. E. McNeil, *Cellulose*, 2012, **19**, 2033–2047.
53 X. Xu, F. Liu, L. Jiang and J. Zhu, *ACS Appl. Mater. Interfaces*, 2013, **5**, 2999–3009.
54 X. Xu, H. Wang, L. Jiang, X. Wang, S. a. Payne, J. Y. Zhu and R. Li, *Macromolecules*, 2014, **47**, 3409–3416.
55 A. Liu, A. Walther, O. Ikkala, L. Belova and L. a. Berglund, *Biomacromolecules*, 2011, **12**, 633–641.
56 H. Yu, Z. Qin, B. Liang, N. Liu, Z. Zhou and L. Chen, *J. Mater. Chem. A*, 2013, **1**, 3938.

57 T. Kunugi, C. Ichinose and A. Suzuki, *J. Appl. Polym. Sci.*, 1986, **31**, 429–439.
58 D. Y. Choi, H. W. Kang, H. J. Sung and S. S. Kim, *Nanoscale*, 2013, **5**, 977–983.
59 HunterLab, 2008, http://barnett-technical.com/HunterLab%20Haze%20Ap.
60 D. Corning, 2015, https://www.dowcorning.com/content/publishedlit/11.
61 C. Wan, X. Qiao, Y. Zhang and Y. Zhang, *Polym. Test.*, 2003, **22**, 453–461.
62 J. Krč, M. Zeman, F. Smole and M. Topič, *J. Appl. Phys.*, 2002, **92**, 749.
63 K. Resch, *Polym. Eng. Sci.*, 2006, 521–531.
64 R. Zhou and T. Burkhart, *J. Appl. Polym. Sci.*, 2010, **115**, 1866–1872.
65 T. Wydeven, *Appl. Opt.*, 1977, **16**, 717–721.
66 Q. G. Gu and Q. L. Zhou, *Eur. Polym. J.*, 1998, **34**, 1727–1733.
67 B. M. R. Galdi, V. Nicolais, L. Di Maio and L. Incarnato, *Packag. Technol. Sci.*, 2008, **21**, 257–268.
68 R. S. Jagadish and B. Raj, *Food Hydrocolloids*, 2011, **25**, 1572–1580.
69 J. Zhang, W. Tu and Z. Dai, *Prog. Org. Coat.*, 2012, **75**, 579–583.
70 A. Hongsingthong, T. Krajangsang, I. A. Yunaz, S. Miyajima and M. Konagai, *Appl. Phys. Express*, 2010, **3**, 051102.
71 J. P. Chem, F. C. Stehling, C. S. Speed and L. Westerman, *Macromolecules*, 1981, **14**, 698–708.
72 A. Dufresne, *Mater. Today*, 2013, **16**, 220–227.
73 J. Wang, Q. Cheng, L. Lin and L. Jiang, *ACS Nano*, 2014, 2739–2745.
74 Y. Okahisa, A. Yoshida, S. Miyaguchi and H. Yano, *Compos. Sci. Technol.*, 2009, **69**, 1958–1961.
75 H.-W. Liang, Q.-F. Guan, Z. Zhu, L.-T. Song, H.-B. Yao, X. Lei and S.-H. Yu, *NPG Asia Mater.*, 2012, **4**, e19.
76 R. Apetz and M. P. B. Van Bruggen, *J. Am. Ceram. Soc.*, 2003, **86**, 480–486.
77 N. Sultanova, S. Kasarova and I. Nikolov, *Acta Phys. Pol., A*, 2009, **116**, 585–587.
78 N. Sultanova and S. Kasarova, *Refract. website*, 2016, http://refractiveindex.info/?shelf=organic&book=ce.
79 R. Boulesteix, A. Maître, L. Chrétien, Y. Rabinovitch and C. Sallé, *J. Am. Ceram. Soc.*, 2013, **96**, 1724–1731.
80 W. Zhang, T. Lu, N. Wei, Y. Wang, B. Ma, F. Li, Z. Lu and J. Qi, *J. Alloys Compd.*, 2012, **520**, 36–41.
81 S. Ye, A. R. Rathmell, Z. Chen, I. E. Stewart and B. J. Wiley, *Adv. Mater.*, 2014, **26**, 6670–6687.
82 J. Lee, S. T. Connor, Y. Cui and P. Peumans, *Nano Lett.*, 2008, **8**, 689–692.
83 J. Zhou, *SEN'I GAKKAISHI*, 2011, **67**, 125–131.
84 J. Zhou, T. Fukawa and M. Kimura, *Polym. J.*, 2011, **43**, 849–854.

